High Rayleigh number convection in a three-dimensional porous medium

Duncan R. Hewitt[1,†], **Jerome A. Neufeld**[1,2,3] **and John R. Lister**[1]

[1]Institute of Theoretical Geophysics, Department of Applied Mathematics and Theoretical Physics,
University of Cambridge, Wilberforce Road, Cambridge CB3 0WA, UK

[2]Bullard Laboratories, Department of Earth Science, University of Cambridge, Cambridge CB3 0EZ, UK

[3]BP Institute, University of Cambridge, Cambridge CB3 0EZ, UK

High-resolution numerical simulations of statistically steady convection in a three-dimensional porous medium are presented for Rayleigh numbers $Ra \leqslant 2 \times 10^4$. Measurements of the Nusselt number Nu in the range $1750 \leqslant Ra \leqslant 2 \times 10^4$ are well fitted by a relationship of the form $Nu = \alpha_3 Ra + \beta_3$, for $\alpha_3 = 9.6 \times 10^{-3}$ and $\beta_3 = 4.6$. This fit indicates that the classical linear scaling $Nu \sim Ra$ is attained, and that Nu is asymptotically approximately 40 % larger than in two dimensions. The dynamical flow structure in the range $1750 \leqslant Ra \leqslant 2 \times 10^4$ is analysed, and the interior of the flow is found to be increasingly well described as $Ra \to \infty$ by a heat-exchanger model, which describes steady interleaving columnar flow with horizontal wavenumber k and a linear background temperature field. Measurements of the interior wavenumber are approximately fitted by $k \sim Ra^{0.52 \pm 0.05}$, which is distinguishably stronger than the two-dimensional scaling of $k \sim Ra^{0.4}$.

Key words: convection, convection in porous media, porous media

1. Introduction

Statistically steady Rayleigh–Bénard convection, driven by a heated lower boundary and a cooled upper boundary, is a canonical fluid-dynamical system which provides a context for the study of nonlinear convective flow and the associated dynamics of pattern formation, instabilities and turbulence (Cross & Hohenberg 1993; Kadanoff 2001). The statistically steady system also allows for accurate measurement of the buoyancy flux, as characterized by the dimensionless Nusselt number Nu, as a function of the Rayleigh number (e.g. Ahlers, Grossmann & Lohse 2009). The Rayleigh number Ra provides a measure of the relative strength of convection, and can be defined as a ratio of the driving buoyancy forces and the dissipative effects of viscosity and diffusion (see § 2).

In this paper, we present a numerical study of statistically steady three-dimensional convection in a Rayleigh–Bénard cell containing a saturated porous medium, which we term a 'Rayleigh–Darcy' cell. A Rayleigh–Darcy cell provides one of the simplest systems for the study of convection, owing to the absence of inertia in Darcy's law.

† Email address for correspondence: drh39@cam.ac.uk

Convection in a porous medium also plays a central role in a range of physical and industrial applications (Nield & Bejan 2006), with particular recent interest in the field stemming from the importance of convection as a mechanism for the long-term storage of geologically sequestered CO_2 (e.g. Metz *et al.* 2005; Bickle 2009; Huppert & Neufeld 2014).

Three-dimensional Rayleigh–Darcy convection remains largely unstudied except at low values of Ra. Two-dimensional Rayleigh–Darcy convection, in contrast, has been explored across a range of values of Ra (Nield & Bejan 2006) and the results of this exploration are briefly reviewed here. For $Ra < 4\pi^2$, there is no flow (Lapwood 1948). For $4\pi^2 < Ra \lesssim 1300$, the flow takes the form of large-scale convective rolls, which, as Ra is increased, are perturbed by a series of boundary-layer 'dripping' instabilities (Graham & Steen 1994). For $Ra \gtrsim 1300$, the quasisteady background rolls are completely broken down by plume-shedding from the boundaries (Otero *et al.* 2004; Hewitt, Neufeld & Lister 2012); this range is known as the 'high-Ra' regime. The flow in the high-Ra regime is characterized in the interior of the cell by persistent vertical exchange flow of columnar megaplumes, which are fed from the upper and lower boundaries by the vigorous mixing of short-wavelength protoplumes. The interior flow is increasingly well described, as $Ra \to \infty$, by a simple 'heat-exchanger' solution, which comprises a steady balance of vertical advection along a weak background temperature gradient and horizontal diffusion between interleaving counterflowing columns (Hewitt *et al.* 2012). Measurements of the average columnar wavenumber k are approximately fitted by $k \sim Ra^{0.4}$ over a range $1300 < Ra \leqslant 4 \times 10^4$. It was recently suggested that the stability of the interior columnar flow provides a physical basis for this relationship, and that the asymptotic scaling is $k \sim Ra^{5/14}$ as $Ra \to \infty$ (Hewitt, Neufeld & Lister 2013*b*). Measurements of the flux $Nu(Ra)$ over the range $1300 < Ra \leqslant 4 \times 10^4$ are extremely well fitted by a relationship of the form $Nu = \alpha_2 Ra + \beta_2$, where $\alpha_2 = 6.9 \times 10^{-3}$ and $\beta_2 = 2.75$ (Hewitt, Neufeld & Lister 2013*a*). This fit indicates that a linear scaling $Nu \sim Ra$ is attained asymptotically, in agreement with the classical scaling argument (following Howard 1964) that the dimensional flux is independent of the height of the cell.

Most previous numerical studies of three-dimensional Rayleigh–Darcy convection have focussed on steady convection for $Ra \lesssim 300$. As in two dimensions, there is no flow for $Ra < 4\pi^2$, while for $4\pi^2 \leqslant Ra \lesssim 4.5\pi^2$ the only unstable mode is purely two-dimensional (Holst & Aziz 1972). The two-dimensional mode continues to give the largest heat flux for $Ra \lesssim 97$ (Straus & Schubert 1979), while for $97 \lesssim Ra \lesssim 300$ the flux is maximized by a steady three-dimensional planform (Schubert & Straus 1979). Multiple possible steady states exist across this range of Ra (Straus & Schubert 1981). Schubert & Straus (1979) found unsteady solutions for $Ra \gtrsim 300$, and some of the dynamics of the flow for $300 \lesssim Ra \lesssim 740$ were investigated by Kimura, Schubert & Straus (1989). We are not aware of any numerical studies of the statistically steady system that explore the dynamics of the flow for $Ra > 740$. More recent numerical studies have explored transient (rather than statistically steady) porous convection in three dimensions, driven by a buoyancy source on one boundary only (Pau *et al.* 2010; Fu, Cueto-Felgueroso & Juanes 2013). The latter authors explored the dynamics of the flow for $Ra \leqslant 6400$ and identified cellular structures of plumes near to the active boundary, which coarsened and were entrained into larger, more persistent, plumes. The spatial scale of the plume structures near the boundary scaled approximately with Ra^{-1}.

Laboratory experiments of statistically steady three-dimensional porous convection have also provided measurements of both the heat flux and the dominant planform

of the flow (Elder 1967; Lister 1990). The detailed experiments of Lister (1990) are particularly interesting as they provide observations of the structure of the flow for $Ra = O(1000)$: the flow consisted of 'a significant number of dendritic downwellings' which fed into larger plumes, and measurements suggested that the lateral scale of the large plumes decreased like $(Ra + c)^{-0.5}$, for some constant c.

In this paper, we investigate in detail the flow in a three-dimensional Rayleigh–Darcy cell for $Ra \leqslant 2 \times 10^4$, using high-resolution numerical simulations. In §2, we outline the governing equations and numerical scheme used in the paper. In §3.1, we briefly describe some features of the flow for $4\pi^2 \leqslant Ra \lesssim 1750$. In §3.2, we explore in detail the dynamical structure of the flow and the buoyancy flux $Nu(Ra)$ in the 'high-Ra' regime ($Ra \gtrsim 1750$). In §4, we summarize and discuss the main results of this work.

2. Governing equations and numerical scheme

2.1. *Dimensionless equations*

We consider a three-dimensional cell of height H containing a fluid-saturated homogeneous and isotropic porous medium. The cell is heated at the lower boundary and cooled at the upper boundary, such that a temperature difference ΔT, which gives rise to a density difference $\Delta\rho$, is imposed across the cell. The flow $\boldsymbol{u} = (u, v, w)$ in the medium is assumed to be incompressible, making the Boussinesq approximation, and satisfies Darcy's law. The equation of state $\rho(T)$ is linear, and the temperature field T evolves by advection and diffusion. In dimensionless variables, these equations are given by

$$\nabla \cdot \boldsymbol{u} = 0, \quad \boldsymbol{u} = -\left(\nabla p + T\hat{\boldsymbol{z}}\right), \tag{2.1a,b}$$

$$\frac{\partial T}{\partial t} = -\boldsymbol{u} \cdot \nabla T + \frac{1}{Ra}\nabla^2 T, \tag{2.2}$$

where p is the pressure. The Rayleigh number Ra is given by

$$Ra = \frac{\Delta\rho g K H}{\phi \kappa \mu}, \tag{2.3}$$

where g is the gravitational acceleration, K is the permeability, ϕ is the porosity, κ is the thermal diffusivity and μ is the viscosity of the fluid, all of which are assumed to be constant. Heat transfer to the solid phase of the medium is neglected. The equations have been non-dimensionalized with respect to the buoyancy–velocity scale $U = \Delta\rho g K / \mu$ and the convective time scale $\phi H / U$. With this choice of dimensionless variables, the Rayleigh number acts as an inverse diffusivity in (2.2).

In dimensionless variables, the Rayleigh–Darcy cell has unit height with boundary conditions on the upper and lower boundaries given by

$$w = 0, \quad T = 1 \quad \text{on } z = 0, \quad w = T = 0 \quad \text{on } z = 1. \tag{2.4a,b}$$

The cell is periodic in the two horizontal directions, with period L (figure 1a).

The average dimensionless flux is given by the Nusselt number,

$$Nu = \langle nu(t) \rangle = \left\langle \frac{1}{L^2} \int_0^L \int_0^L -\left.\frac{\partial T}{\partial z}\right|_{z=0} \mathrm{d}x\,\mathrm{d}y \right\rangle, \tag{2.5}$$

where the angle brackets $\langle\,\rangle$ denote a long-time average and $nu(t)$ is the instantaneous horizontally averaged Nusselt number.
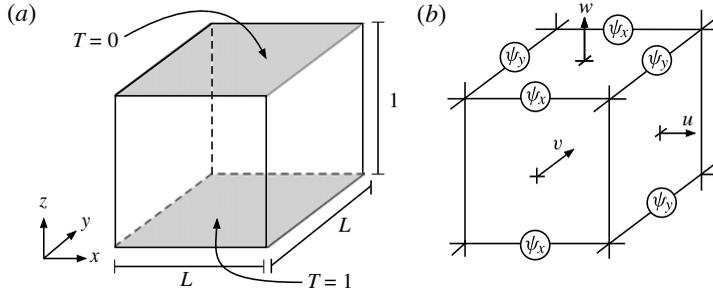
FIGURE 1. (*a*) A schematic diagram of the dimensionless Rayleigh–Darcy cell under consideration. All four side boundaries are periodic. (*b*) One cuboid of the numerical grid (see §2.2), with the locations at which ψ_x and ψ_y are calculated. The components of the velocity $(u, v, w) = \nabla \times (\psi_x, \psi_y, 0)$ are thus determined at the centre of each face of the cuboid. The temperature is calculated at the centre of each cuboid. The advective flux is calculated at the centre of each face of the cuboid using the velocity there and the average of the neighbouring temperatures.

2.2. *Numerical method*

The constraint of incompressibility (2.1*a*) can be satisfied by the introduction of a vector potential $\boldsymbol{\Psi} = (\psi_x, \psi_y, \psi_z)$ which obeys $\boldsymbol{u} = \nabla \times \boldsymbol{\Psi}$. The potential is determined by this relationship only up to the addition of $\nabla \xi$, for any scalar ξ. To constrain this gauge freedom, we consider the curl of (2.1*b*), which gives

$$\nabla \times \boldsymbol{u} = \nabla \left(\nabla \cdot \boldsymbol{\Psi} \right) - \nabla^2 \boldsymbol{\Psi} = \left(\frac{\partial T}{\partial y}, -\frac{\partial T}{\partial x}, 0 \right). \tag{2.6}$$

Equation (2.6) reduces to a set of simple Poisson equations for the components $\psi_{x,y,z}$ of the vector potential if the gauge condition is chosen to be

$$\nabla \cdot \boldsymbol{\Psi} = 0, \tag{2.7}$$

(cf. the Lorentz gauge condition in electrodynamics). Equation (2.6) then reduces to

$$\nabla^2 \psi_x = -\frac{\partial T}{\partial y}, \quad \nabla^2 \psi_y = \frac{\partial T}{\partial x}, \quad \nabla^2 \psi_z = 0. \tag{2.8a–c}$$

It is straightforward to show (see E & Liu (1997)) that the gauge condition (2.7) is satisfied throughout the domain provided that it is satisfied on the boundaries. Since the domain is periodic in both *x* and *y*, both the gauge condition (2.7) and the velocity boundary conditions in (2.4) are satisfied by setting

$$\psi_x = \psi_y = \frac{\partial \psi_z}{\partial z} = 0, \quad \text{on } z = 0, 1. \tag{2.9a–c}$$

Equations (2.8*c*) and (2.9*c*) combine to give $\psi_z = 0$ everywhere. The velocity $\boldsymbol{u}$ is determined by the Poisson equations (2.8*a,b*) for ψ_x and ψ_y, with boundary conditions (2.9*a,b*).

We solved (2.2) and (2.8*a,b*) numerically, using a coordinate transformation $\zeta(z)$ to fully resolve the thin diffusive boundary layers near the upper and lower boundaries of the domain. The Poisson equations (2.8*a,b*) were solved using fast Fourier transforms for the *x* and *y* derivatives, and second-order finite differences for the vertical

derivatives. The transport equation (2.2) was solved using an unconditionally stable three-dimensional alternating-direction implicit method, following Brian (1961). We spatially discretized the diffusion terms using second-order finite differences, and used a flux-conservative approach for the advection operator, which was aided by a staggered numerical grid for ψ_x, ψ_y and T (see figure 1b). A midpoint method was used for the time derivatives to give second-order temporal accuracy. The numerical scheme was parallelized using a hybrid of open multi-processing (OpenMP) and message-passing interface (MPI) specifications.

We verified our numerical scheme by reproducing published measurements of $Nu(Ra)$ for $Ra < 300$ (Schubert & Straus 1979). For simulations at larger values of Ra, the horizontal resolution was chosen to fully resolve the smallest horizontal scales, which appear to decrease roughly like Ra^{-1}, and the vertical scale was chosen to ensure that enough grid points lay inside the thin boundary layers near $z = 0, 1$. The temporal resolution was chosen to satisfy the Courant condition. Typical values of the horizontal and (transformed) vertical discretizations range from $\Delta x = \Delta y = (128)^{-1}$ and $\Delta \zeta = (150)^{-1}$ at $Ra = 1000$, to $\Delta x = \Delta y = (2048)^{-1}$ and $\Delta \zeta = (220)^{-1}$ at $Ra = 2 \times 10^4$. We tested simulations with double the horizontal resolution and with both larger and smaller vertical resolutions at $Ra = 2000$ and recovered statistically identical results. The temporal discretization was typically $\Delta t = 3\Delta x$.

Except for some simulations described in §3.1, the initial condition was given by a linear vertical temperature gradient, $T(x, y, z) = 1 - z$, with a spatially random perturbation of magnitude 2.5×10^{-3}. We refer to this initial condition as IC1.

3. Numerical results

The primary focus of this paper is to explore three-dimensional flow in the 'high-Ra' regime, which will be taken here to be the range $Ra \gtrsim 1750$. In order to provide a context for these results, we begin in §3.1 with a brief outline of the dynamics of the flow in the 'moderate-Ra' regime $Ra \lesssim 1750$. In §3.2, we investigate the high-Ra regime in detail.

3.1. *Overview of the flow dynamics for moderate values of Ra*

Two sets of simulations for moderate Ra were undertaken with aspect ratio $L = 2$. The first set comprised independent simulations in which the initial conditions were given by a small random perturbation to a linear base state (IC1). The second set was a sequence of simulations in which the final state of one simulation was used as the initial condition for the next and Ra was increased by a factor of 6/5 (IC2). In each case, the simulations were allowed to run until the flow had evolved to a steady or statistically steady state.

Figure 2(a) shows measurements of $Nu(Ra)$ from these simulations. It can be seen that there is some variability, both between repeated simulations with IC1 at the same value of Ra, and between the two sets of simulations at comparable values of Ra. This variability is due to the flow having evolved to different spatial structures in different simulations, rather than to insufficient averaging of the heat flux in a given simulation.

In the simulations with IC1 (figure 2a, circles), the spatial structure of the flow was as follows. For $45 \lesssim Ra \lesssim 100$, the flow evolved to a steady planform of strictly two-dimensional rolls (figure 2b; i). For $100 \lesssim Ra \lesssim 225$, the flow instead evolved to a steady planform of inclined rolls (figure 2b; ii), where 'inclined' means not aligned with either axis. For $225 \lesssim Ra \lesssim 400$, the flow evolved to a steady diamond planform, which consisted of two diagonally aligned square cells (figure 2b; iii). At $Ra = 400$,
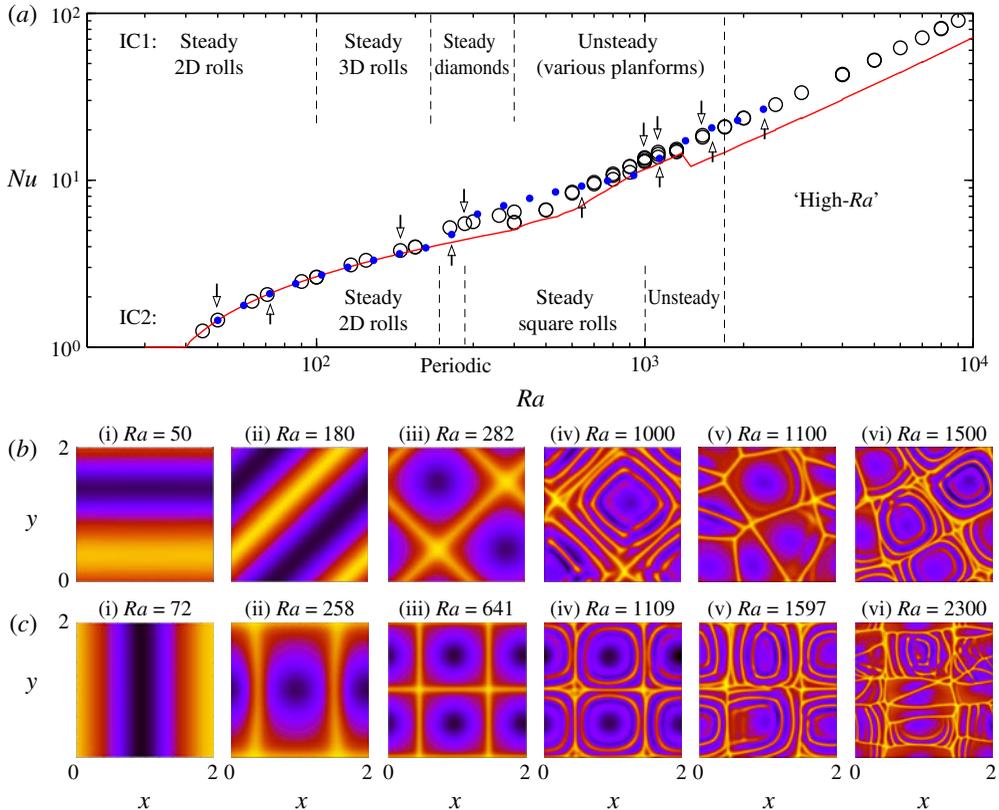
FIGURE 2. (Colour online) (*a*) Measurements of *Nu*(*Ra*) from the onset of convection at $Ra = Ra_{crit} = 4\pi^2$ to the 'high-*Ra*' regime. Measurements are shown from simulations with initial conditions IC1 (black circles) and IC2 (blue dots), as described in the text. All simulations with $Ra \leqslant 1750$ have aspect ratio $L = 2$; those with $Ra \geqslant 1750$ are discussed in §3.2. The relationship *Nu*(*Ra*) from a two-dimensional cell (with $L = 2$ and IC2), taken from Hewitt *et al.* (2012), is included for comparison (red line). (*b*,*c*) Snapshots of the temperature field at depth $z = 30/Ra$, just above the lower boundary, for a selection of values of *Ra*, corresponding to the small arrows in (*a*). The snapshots in (*b*) are of simulations with IC1 (down arrows), and those in (*c*) are of simulations with IC2 (up arrows).

one simulation again evolved to a steady diamond planform, while another evolved to an unsteady square planform.

For $400 \lesssim Ra \lesssim 1750$, the flow was unsteady, and we found a variety of spatial structures in this range. In most simulations (e.g. figure 2*b*; iv, vi), the flow evolved to a regular background planform of convective cells on which were superposed unsteady sheet-like 'dripping' disturbances arising in the boundary layers. In a few simulations (e.g. figure 2*b*; v), the flow appeared more disordered and a regular background planform was not evident. For $Ra \gtrsim 1750$, we did not observe any regular planform. In addition, as can be seen in figure 2(*a*), for $Ra \gtrsim 1750$ we did not find any significant variability in *Nu* between different simulations with IC1. Hence, we refer to the range $Ra \gtrsim 1750$ as the high-*Ra* regime.

We found some significant differences in the spatial structure of the flow between the simulations with IC1 and simulations with IC2 at comparable values of *Ra*. In the

simulations with IC2 (figure 2*a*, dots), the spatial structure was as follows. For $50 \leqslant Ra \leqslant 215$, the planform of the flow was a steady two-dimensional roll (figure 2*c*; i). At $Ra = 258$ the flow evolved to an unsteady state which oscillated periodically between two rectangular cells (figure 2*c*; ii) and one diagonally aligned square cell. For $310 \leqslant Ra \leqslant 924$, the planform was a steady array of four square cells (figure 2*c*; iii). For $1109 \leqslant Ra \leqslant 2300$, the flow took the form of unsteady perturbations to these regular background cells, and the structure of the flow appeared to be increasingly disordered as Ra was increased through this range (figure 2*c*; iv–vi).

Comparison of the two sets of simulations outlined above indicates that hysteresis can affect both the flow structure and the value of Nu for $Ra \lesssim 1750$. The results also suggest that the bifurcation structure and the dynamical behaviour of the system are highly complex in this moderate-Ra regime, and would require a detailed further study to disentangle. For example, for each of the different spatial structures of the flow identified in the simulations with IC1, a branch of solutions could presumably be followed for increasing or decreasing Ra as in the simulations with IC2. However, since the aim of this paper is to explore the high-Ra regime, such a detailed exploration is left for the future.

3.2. *The high-Ra regime*

As discussed above, for $Ra \geqslant 1750$ we found that there is no significant variation in Nu between different simulations with IC1 at the same Ra, and the flow structure did not exhibit any regular background planform. In this section, we investigate the flow in the high-Ra regime in detail. All the simulations presented in the remainder of this paper have initial conditions IC1.

3.2.1. *Structure of the flow*

Figure 3 shows snapshots of the temperature field in the high-Ra regime at different depths z and different values of Ra, and figure 4 shows snapshots from the same simulations at fixed $x = L/2$. The flow has many analogues with two-dimensional Rayleigh–Darcy flow at high Ra; in particular, there are clear visual parallels between the vertical slices in figure 4 and snapshots of the flow in two dimensions (Otero *et al.* 2004; Hewitt *et al.* 2012). The flow can be divided into three regions of differing dynamics. The interior region appears to be dominated by roughly vertical and fairly large-scale exchange flow in distinct columns of hot rising fluid and cold sinking fluid, which we refer to as megaplumes. At the upper and lower boundaries of the domain there are thermal boundary layers which are almost too small to distinguish in figure 4. Between the boundary layers and the interior flow is a region dominated by the growth and interaction of long, thin, sheet-like plume structures that arise from time-dependent boundary-layer instabilities (figure 3). The sheet-like plumes are the three-dimensional analogue of two-dimensional protoplumes (Hewitt *et al.* 2012), and so we refer to this region as the protoplume region. The protoplume sheets erupt from the boundary layers and are laterally entrained into the large-scale megaplume flow. Visual inspection of figure 3 suggests that the spatial scale of the protoplumes decreases roughly like Ra^{-1} (note the different spatial scales in the figure), while the dominant length scale of the interior megaplumes has a much weaker dependence on Ra (see § 3.2.4 below).

3.2.2. *The Nusselt number Nu(Ra)*

In a statistically steady state in the high-Ra regime, the time-dependent Nusselt number, $nu(t)$, exhibits chaotic fluctuations about the time-averaged value Nu.
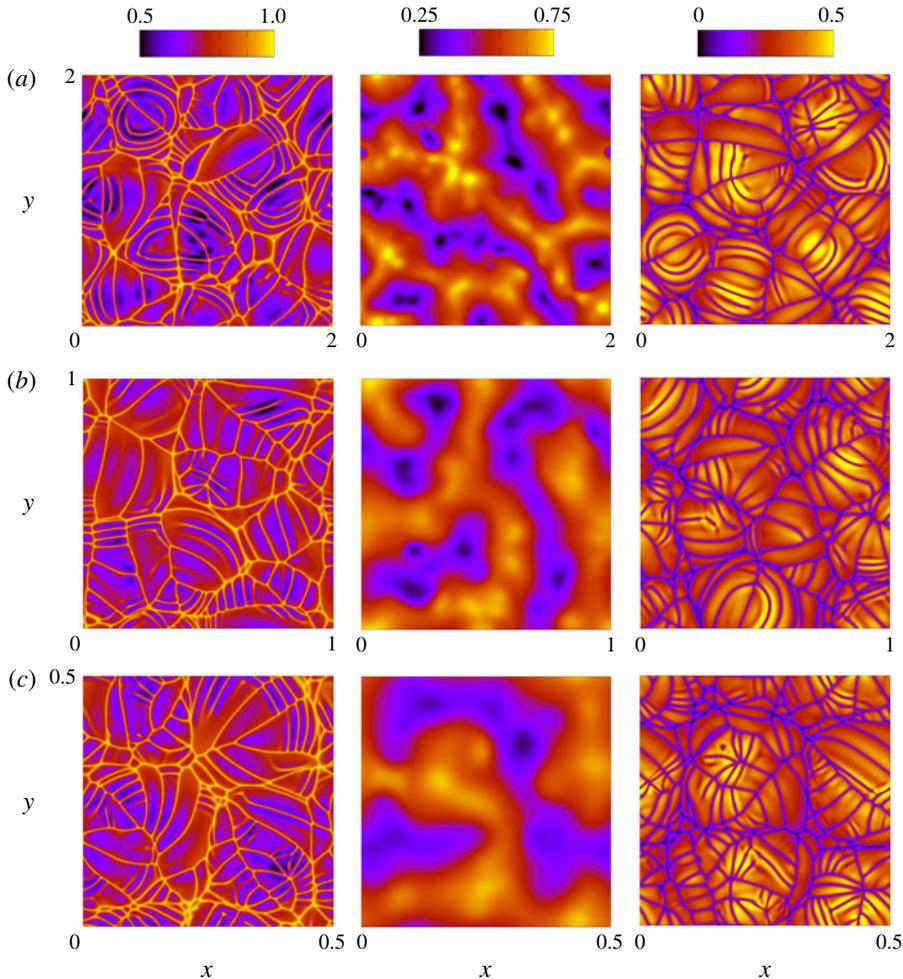
FIGURE 3. (Colour online) Snapshots of the temperature field at heights of $z = 30/Ra$ near to the lower boundary (left), $z = 0.5$ in the interior of the flow (centre), and $z = 1 - 30/Ra$ near to the upper boundary (right). (*a*) $Ra = 4000$ and $L = 2$; (*b*) $Ra = 8000$ and $L = 1$; and (*c*) $Ra = 1.6 \times 10^4$ and $L = 0.5$. Note the different scales on the axes for each subfigure.

The amplitude of the fluctuations is notably smaller than that measured for two-dimensional porous convection at the same values of Ra (figure 5), which is likely a reflection of the additional spatial dimension over which the flux is averaged. The time-averaged Nusselt number $Nu = \langle nu \rangle$ is estimated numerically by time-averaging $nu(t)$ until the uncertainty in the mean is less than 0.25 %. In a typical simulation, this averaging takes place over a dimensionless time of between 300 and 500.

Measurements of $Nu(Ra)$ for different aspect ratios L in the high-Ra regime are shown in figure 6, together with the least-squares power-law and linear (i.e. first-order polynomial) fits to the data. The best-fit power-law scaling is $Nu \sim Ra^{0.94}$, but we find that the data is much more accurately described by the linear fit, which takes the form

$$Nu = \alpha_3 Ra + \beta_3; \quad \alpha_3 = 9.6 \times 10^{-3}, \quad \beta_3 = 4.6. \tag{3.1}$$

The good fit given by (3.1) strongly suggests that, as in two dimensions, the classical linear scaling $Nu \sim Ra$ is attained asymptotically.
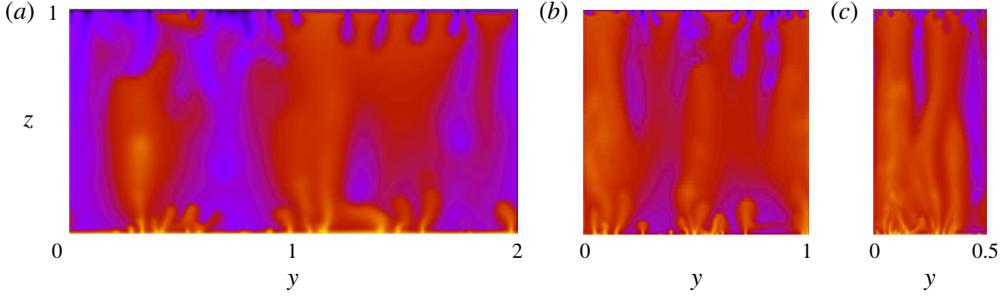
FIGURE 4. (Colour online) Snapshots of the temperature field (from the same simulations as in figure 3) at $x = L/2$, for (a) $Ra = 4000$ and $L = 2$; (b) $Ra = 8000$ and $L = 1$; and (c) $Ra = 1.6 \times 10^4$ and $L = 0.5$.
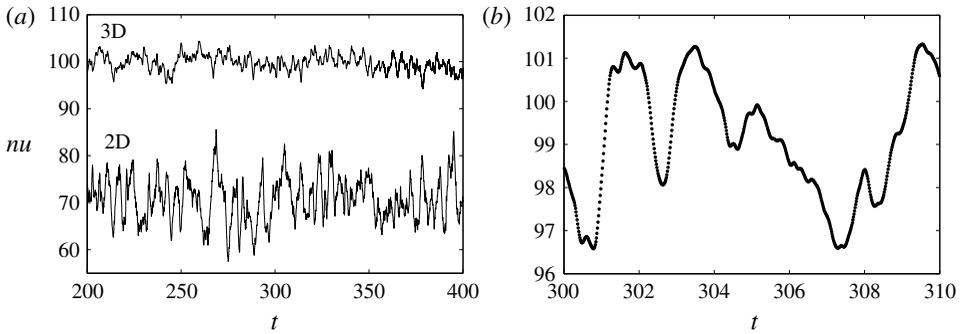
FIGURE 5. The instantaneous horizontally averaged Nusselt number $nu(t)$ for $Ra = 10^4$ and $L = 1$: (a) together with $nu(t)$ from numerical simulations of two-dimensional Rayleigh–Darcy convection at $Ra = 10^4$ (lower line); and (b) individual data points separated by five time steps Δt, which illustrates the high temporal resolution of the calculations.
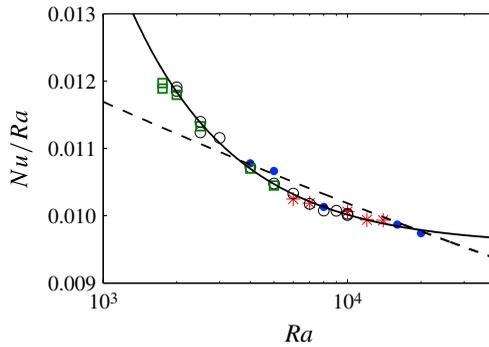
FIGURE 6. (Colour online) The time-averaged Nusselt number scaled by Ra, in the high-Ra regime, for aspect ratios $L = 2$ (green squares), $L = 1$ (black circles), $L = 0.75$ (red stars) and $L = 0.5$ (blue dots). The best-fit power law $Nu = 0.018Ra^{0.94}$ (dashed line) does not capture the trend in the data as Ra is increased; instead, a very good fit is provided by $Nu = \alpha_3 Ra + \beta_3$ (solid line) for $\alpha_3 = 9.6 \times 10^{-3}$ and $\beta_3 = 4.6$.

While (3.1) has an analogous form to the linear fit found for two-dimensional porous convection (Hewitt *et al.* 2013*a*), perhaps the most important practical observation from these measurements is that the flux $Nu(Ra)$ is much larger than in two dimensions. A comparison of the pre-factor $\alpha_3 = 9.6 \times 10^{-3}$ from (3.1) with the pre-factor $\alpha_2 = 6.9 \times 10^{-3}$ from the two-dimensional fit gives $\alpha_3/\alpha_2 \approx 1.4$, which indicates that the flux in the high-Ra regime is approximately 40 % larger in three dimensions.

The slight variation in the measurements shown in figure 6 is likely a reflection of some long time-scale variability in the structure of the flow in the interior of the domain. It is possible that the structure is affected by mode restriction from the horizontal periodicity of the domain, although the relatively good agreement between measurements at different aspect ratios in figure 6 suggests that any effects of mode restriction on Nu are small. We return to this point when we investigate the dominant horizontal length scales of the flow in § 3.2.4 below.

3.2.3. *Three-dimensional heat-exchanger solution*

Movies of the flow through the interior of the domain reveal that the large-scale exchange flow is almost quasi-steady: the upwelling and downwelling plumes are 'persistent', in that their locations do not vary appreciably over either the time scale for eruption and entrainment of sheet-like protoplumes, or over the time scale for vertical advection across the domain.

As in two dimensions (Hewitt *et al.* 2012), there are steady 'heat-exchanger' solutions to the governing equations (2.1) and (2.2) which can be used as a model for the exchange flow in the interior of the domain. Heat-exchanger solutions comprise a steady balance between vertical advection along a background temperature gradient and horizontal diffusion between interleaving columns of a given planform. The simplest such three-dimensional heat-exchanger model, with a square columnar planform, is given by

$$T = A \cos kx \cos ky - \frac{2k^2}{Ra}z, \quad u = v = 0, \quad w = A \cos kx \cos ky, \qquad (3.2a\text{–}c)$$

and consists of square columns with amplitude A and wavenumber k in both x and y directions.

Measurements of the temporally and horizontally averaged temperature $\overline{T}$ (figure 7) show that the background temperature is roughly linear throughout the interior region, in agreement with the prediction of (3.2*a*). However, unlike in two dimensions, where the gradient decreases with Ra (Hewitt *et al.* 2012), here we observe that the magnitude of the weak negative gradient increases as Ra is increased. We return to this observation in § 3.2.5.

We measure the amplitude using the root-mean-squared (r.m.s.) temperature perturbations and velocities, T_{rms}, w_{rms}, v_{rms} and u_{rms}. Analytic calculation of the r.m.s. values from (3.2) shows that, in the heat-exchanger model, $T_{rms} = w_{rms} = A/2$ and $u_{rms} = v_{rms} = 0$. Numerical measurements of the r.m.s. quantities at $z = 0.5$ indicate an increasing agreement with the model predictions as Ra is increased (figure 8*a*). The horizontal velocities decrease with Ra, and the vertical velocity and temperature appear to tend to the same constant value, which yields an estimate of $A = 2T_{rms} \approx 0.2$. As a consistency check, this measurement can be used with the heat-exchanger theory to estimate the flux $Nu(Ra)$, as follows. As $Ra \to \infty$, vertical advection dominates the flux through the interior of the domain, and the vertical advective flux given by (3.2) is $Nu = A^2Ra/4$. Using the measured estimate of A gives a prediction of $Nu \approx 0.01Ra$,
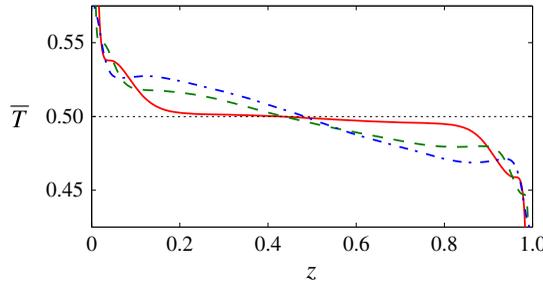
FIGURE 7. (Colour online) The temporally and horizontally averaged temperature profile $\overline{T}$, for $Ra = 4000$ (red solid), $Ra = 8000$ (green dashed) and $Ra = 1.6 \times 10^4$ (blue dot-dashed). The profiles are approximately linear through the interior of the domain, and the gradient increases with Ra. In contrast, for two-dimensional Rayleigh–Darcy convection the gradient decreases with Ra (Hewitt *et al.* 2012). The thin dotted line shows $\overline{T} = 0.5$.
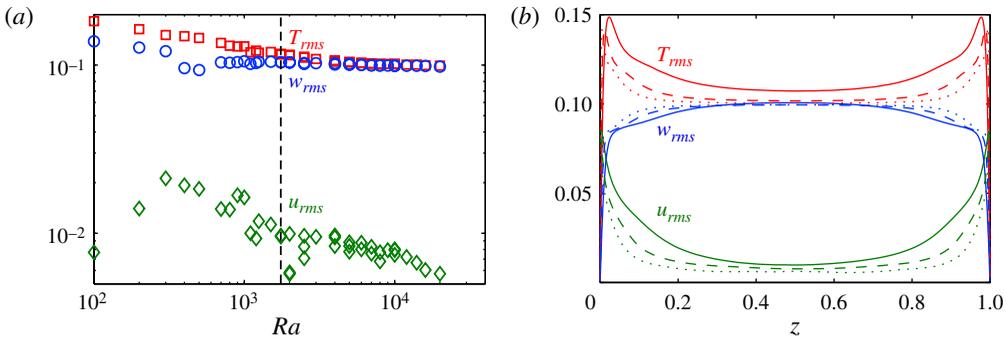
FIGURE 8. (Colour online) Measurements of the time-averaged r.m.s. temperature perturbations T_{rms} and velocities w_{rms} and u_{rms} (*a*) at $z = 0.5$, against Ra (the dashed line indicates the start of the high-Ra regime at $Ra \approx 1750$); and (*b*) for $Ra = 4000$ and $L = 2$ (solid), $Ra = 8000$ and $L = 1$ (dashed), and $Ra = 1.6 \times 10^4$ and $L = 0.5$ (dotted), against z. Measurements of v_{rms} are indistinguishable from u_{rms}, and so are not shown.

which is reassuringly close to the asymptotic prediction from the directly measured relationship (3.1) of $Nu = 9.6 \times 10^{-3} Ra$.

Figure 8(*b*) shows the vertical variation of the r.m.s. measurements at different values of Ra. The figure indicates that the r.m.s. quantities are increasingly uniform throughout the interior of the domain as Ra is increased, in agreement with the heat-exchanger model. In contrast, near the upper and lower boundaries the r.m.s. quantities vary appreciably. These measurements reflect the fact that the heat-exchanger model breaks down near the boundaries where the flow is dominated by the strongly time-dependent growth and entrainment of sheet-like protoplumes.

These measurements all indicate that a heat-exchanger model provides an increasingly good description as $Ra \to \infty$ of the flow throughout the interior region of a three-dimensional Rayleigh–Darcy cell. As in two dimensions, the interior flow becomes increasingly ordered as $Ra \to \infty$ into columns of steady exchange flow, although the planform of this flow is not yet clear. Some indication of the lateral structure is provided by measurements of the dominant horizontal wavenumber k, which are presented in the next section.
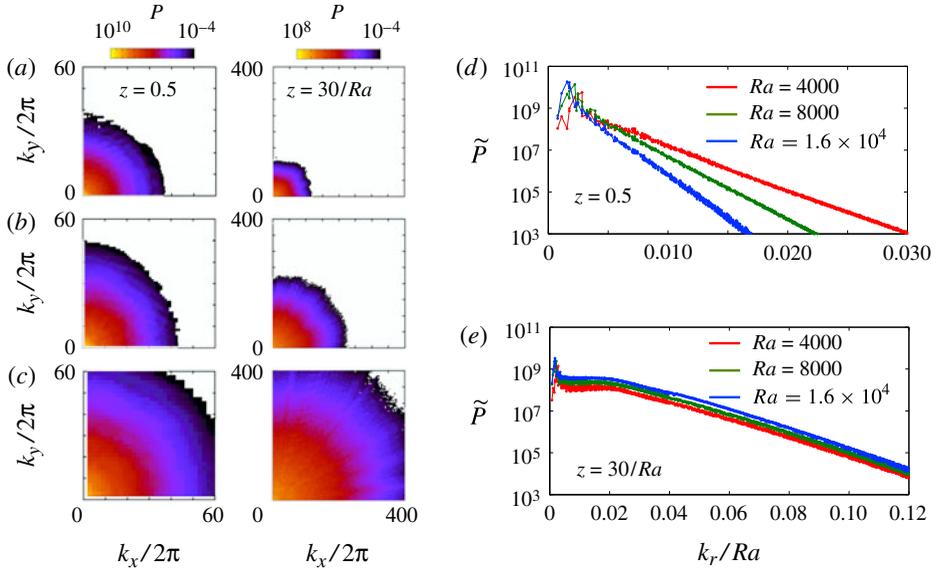
FIGURE 9. (Colour online) (*a–c*) Snapshots of power spectra $P(k_x, k_y)$ at $z = 0.5$ (left) and $z = 30/Ra$ in the protoplume region (right): (*a*) $Ra = 4000$ and $L = 2$; (*b*) $Ra = 8000$ and $L = 1$; and (*c*) $Ra = 1.6 \times 10^4$ and $L = 0.5$. The colour scale is logarithmic. (*d,e*) The radial power $\widetilde{P} = \int Pk_r \mathrm{d}\theta$, where $\theta = \tan^{-1}(k_y/k_x)$, against the radial wavenumber $k_r = (k_x^2 + k_y^2)^{1/2}$ scaled by Ra: (*d*) at $z = 0.5$; and (*e*) at $z = 30/Ra$. Note the different scales on the horizontal axis in (*d*) and (*e*): the clear peak in the power is at the same wavenumber in each figure, which is the dominant horizontal wavenumber of the megaplume flow.

3.2.4. *The average horizontal wavenumber k(Ra)*

In order to extract a measure of the average horizontal wavenumber $k(Ra)$ from the numerical calculations, we measured the power in each mode by taking a two-dimensional Fourier transform of the temperature field. Figure 9(*a–c*) shows snapshots of the resultant power spectra as a function of the horizontal wavenumbers k_x and k_y, both at $z = 0.5$ (in the interior region) and at $z = 30/Ra$ (taken as a rough estimate of a depth in the protoplume region). The spectra reveal that the power $P(k_x, k_y)$ depends predominantly on the magnitude of the wavevector, or the 'radial wavenumber' $k_r = (k_x^2 + k_y^2)^{1/2}$, rather than on the angle $\theta = \tan^{-1}(k_y/k_x)$, which indicates that the flow is isotropic.

Measurements of the radial power $\widetilde{P}(k_r) = \int Pk_r \mathrm{d}\theta$ at $z = 0.5$ (figure 9*d*) show a clear peak in the spectra, which indicates that the flow in the interior of the cell has a well-defined dominant horizontal length scale. This length scale corresponds to the megaplume spacing. For larger radial wavenumbers, there is a rapid exponential decay in the radial power. Measurements of $\widetilde{P}$ at $z = 30/Ra$ (figure 9*e*) again show a peak at the same wavenumber as in the interior, which is the signal from the roots of the megaplumes. For larger radial wavenumbers, however, there is a plateau in the radial power and then a much slower exponential decay than in the interior. These features are due to the high-wavenumber sheet-like plumes that dominate the flow in the protoplume region.

The decay in the radial power also displays a different dependence on Ra in the protoplume region and in the interior of the cell. In the protoplume region (figure 9*e*),
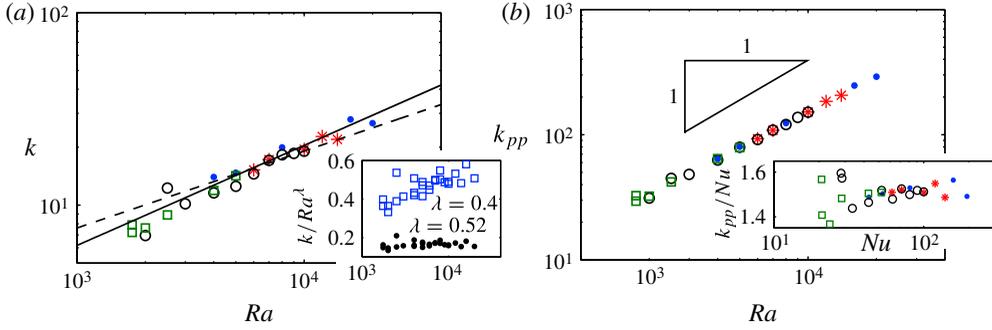
FIGURE 10. (Colour online) Measurements of the average horizontal wavenumber $\bar{k}$ as defined by (3.3). (a) The average interior wavenumber $k = \bar{k}|_{z=0.5}$ from simulations with $L = 2$ (green squares), $L = 1$ (black circles), $L = 0.75$ (red stars) and $L = 0.5$ (blue dots). The solid line is the best-fit power law $k \approx 0.17 Ra^{0.52}$. For comparison, the dashed line is the approximate fit $k \approx 0.48 Ra^{0.4}$ for two-dimensional Rayleigh–Darcy convection (Hewitt *et al.* 2012). The inset shows the measurements scaled by Ra^{λ} for two different trial exponents λ. (b) The average horizontal wavenumber $k_{pp} = \bar{k}|_{z=30/Ra}$ in the protoplume regions. The inset graph of k_{pp}/Nu against Nu points to a linear scaling $k_{pp} \sim Nu$.

the measurements collapse as a function of k_r/Ra, while in the interior (figure 9d) the dependence on Ra is much weaker. The different scaling with Ra of the decay in the power can also be observed in the snapshots of $P(k_x, k_y)$ in figure 9(a–c), where the typical radii of the spectra increase more rapidly with Ra in the protoplume region (right-hand column) than in the interior region (left-hand column).

We measured the average dominant wavenumber $\bar{k}$ at a given height z by taking the expected value of k_r over two dimensions, and averaging over time, to give

$$\bar{k} = \left\langle \frac{\int k_r \widetilde{P}(k_r)\, \mathrm{d}k_r}{\int \widetilde{P}(k_r)\, \mathrm{d}k_r} \right\rangle = \left\langle \frac{\iint \sqrt{k_x^2 + k_y^2}\, P(k_x, k_y)\, \mathrm{d}k_x\, \mathrm{d}k_y}{\iint P(k_x, k_y)\, \mathrm{d}k_x\, \mathrm{d}k_y} \right\rangle. \tag{3.3}$$

We estimate the average horizontal wavenumber k of the interior columnar flow by $k = \bar{k}|_{z=0.5}$. Measurements of $k(Ra)$ are shown in figure 10(a). A least-squares power-law fit to the data gives a scaling of

$$k \approx 0.17\, Ra^{0.52}, \tag{3.4}$$

with 95 % confidence intervals for the exponent giving a range of 0.52 ± 0.05. Equation (3.4) can be compared with the fit $k \approx 0.48 Ra^{0.4}$ to the average wavenumber from two-dimensional Rayleigh–Darcy convection (Hewitt *et al.* 2012): while the magnitude of the wavenumbers is similar over the range of Ra for which we have measurements, the three-dimensional wavenumber displays a distinctly stronger scaling with Ra (figure 10a).

We estimate the average horizontal wavenumber k_{pp} in the protoplume regions by $k_{pp} = \bar{k}|_{z=30/Ra}$. Measurements of $k_{pp}(Ra)$ are shown in figure 10(b). The inset reveals a linear scaling $k_{pp} \sim Nu$, which, from (3.1), implies that $k_{pp} \sim Ra$ as $Ra \to \infty$. This result suggests that the horizontal length scale of the sheet-like protoplumes scales with the boundary-layer depth $\sim 1/Nu$. It also confirms that the average horizontal

length scale of the flow has a much stronger scaling with Ra near to the upper and lower boundaries than in the interior, in agreement both with the different decay of the spectra in figure 9 and with visual comparison of the snapshots in figure 3. In addition, the result agrees with previous suggestions for the Ra^{-1} scaling of protoplume structures in transient three-dimensional convection with only one active boundary (Fu *et al.* 2013).

Owing to the high numerical cost of the calculations, we needed to reduce the aspect ratio L as Ra was increased. It might, therefore, be possible that mode restriction due to the relatively small aspect ratios could have affected the structure of the flow, and thus the measurements of k in figure 10(a). To investigate the effect of mode restriction, we undertook multiple calculations at different aspect ratios across a range of Ra. The good agreement between the corresponding measurements of k (figure 10a) suggests that any effects of mode restriction are small. As an additional check, we undertook two simulations in cells with rectangular, rather than square, horizontal cross-section, and found no statistically significant difference in the measurements of k; these simulations were at $Ra = 2500$ with horizontal aspect ratio 2×1, and $Ra = 5000$ with horizontal aspect ratio 1×0.5. Owing to the high computational cost of simulations at the largest values of Ra, we have been unable to check the results for $Ra \geqslant 1.2 \times 10^4$ at different aspect ratios; however, the data agrees with the trend of the measurements at lower Ra, which again suggests that mode restriction does not play a major role. We note that there is some variability in the data between the different simulations, which does not appear to have a systematic dependence on aspect ratio, and which we attribute to very long time-scale variations in the dominant wavenumber. Similar variability is observed in two-dimensional convection (Hewitt *et al.* 2012).

3.2.5. *The vertical temperature gradient*

In figure 7, we observed that the magnitude of the linear background temperature gradient increased with Ra, particularly between $Ra = 4000$ and $Ra = 8000$. Figure 11(a) shows direct measurements of the background temperature gradient $\partial \overline{T}/\partial z$. The measurements can be approximately divided into two regions of different behaviour: for $Ra \lesssim 5000$ the magnitude of the gradient increases with Ra, while for $Ra \gtrsim 5000$ the gradient is roughly independent of Ra.

The heat-exchanger framework (3.2) indicates that the background temperature gradient is related to the horizontal wavenumber k by

$$\frac{\partial \overline{T}}{\partial z} = -\frac{2k^2}{Ra}. \tag{3.5}$$

Therefore, based on (3.5), the roughly constant temperature gradient for $Ra \gtrsim 5000$ is consistent with the measured scaling $k \sim Ra^{0.52 \pm 0.05}$ for the wavenumber. Indeed, a direct comparison of the measurements of k and measurements of the gradient using (3.5) gives very good agreement for $Ra \gtrsim 5000$ (figure 11b). This agreement provides further evidence that the interior flow is increasingly well described by the heat-exchanger model.

The precise trend in the measurements of the background temperature gradient as $Ra \to \infty$ is not clear from the data in figure 11(a). However, we would not expect a positive asymptotic scaling, since the gradient should not diverge as $Ra \to \infty$. Given the good agreement between the measurements and the heat-exchanger model, this expectation corresponds, via (3.5), to a constraint that the asymptotic exponent for
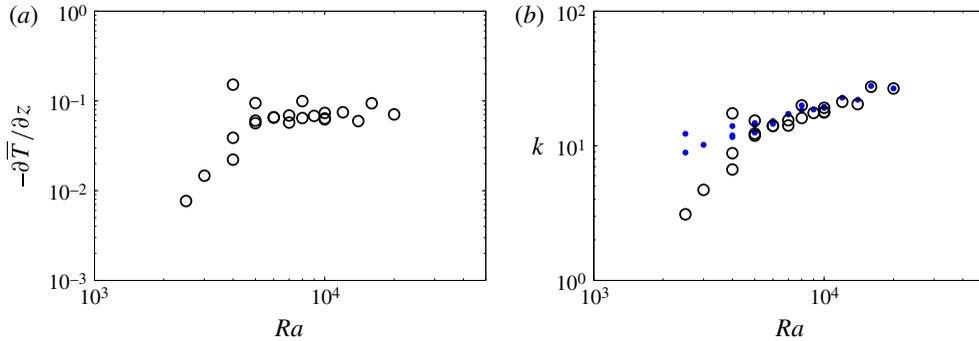
FIGURE 11. (Colour online) (*a*) Measurements of the background temperature gradient $-\partial \overline{T}/\partial z$, as defined by the slope of a linear fit to the measurements of $\overline{T}$ for $0.45 \leqslant z \leqslant 0.55$. (*b*) Comparison of direct measurements of the interior wavenumber k from figure 10(*a*) (dots) and the prediction $k = [(-\partial \overline{T}/\partial z)Ra/2]^{1/2}$ from the measurements in (*a*) and heat-exchanger theory (3.5) (circles).

the scaling of the wavenumber k is no greater than 0.5. It should be noted that 0.5 lies well within the 95%-confidence interval for the exponent in (3.4), and so an asymptotic scaling of $k \sim Ra^{0.5}$ is consistent with the measurements presented here. Measurements at higher values of Ra would be required to confirm this scaling.

4. Conclusions and discussion

We have presented the first measurements of statistically steady three-dimensional convection in a porous medium at high Ra. Measurements of the flux over the range $1750 \leqslant Ra \leqslant 2 \times 10^4$ are very well fitted by an expression of the form $Nu = \alpha_3 Ra + \beta_3$, with $\alpha_3 = 9.6 \times 10^{-3}$ and $\beta_3 = 4.6$. This fit, which has the same form as the corresponding fit for two-dimensional high-Ra porous convection (Hewitt *et al.* 2013*a*), indicates that the flux attains the classical linear scaling asymptotically. The flux is roughly 40% larger than in two dimensions, and this difference has evident importance for physical applications.

The structure of the flow for $Ra \gtrsim 1750$ is dominated in the interior by persistent columnar exchange flow. Instabilities in the thin thermal boundary layers near the upper and lower boundaries give rise to eruptions of long, thin, sheet-like protoplume structures, which are entrained laterally into the interior exchange flow. Measurements of the wavenumber in the protoplume region show that the lateral length scale of the thin sheet-like plumes scales with Nu^{-1}, and thus with Ra^{-1} as $Ra \to \infty$.

Measurements of the interior flow indicate that it is increasingly well described by a steady three-dimensional heat-exchanger flow as Ra is increased. This flow consists of a steady balance of vertical advection in interleaving columns along a background linear temperature gradient and horizontal diffusion between the columns. While we considered a specific heat-exchanger model with a square planform, it is difficult to discern a regular horizontal planform of the exchange flow from snapshots of the interior flow (figure 3). Measurements of the interior flow reveal a distinct average horizontal wavenumber k, which is fitted over the range $1750 \leqslant Ra \leqslant 2 \times 10^4$ by $k \sim Ra^{0.52 \pm 0.05}$. This scaling is much weaker than the scaling in the protoplume regions, but is also distinctly stronger than the corresponding scaling of $k \sim Ra^{0.4}$ in two dimensions. The fairly good agreement between simulations at different aspect

ratios suggests that mode restriction does not have a significant effect on this scaling. In addition, measurements of the background temperature gradient for $Ra \gtrsim 5000$ are consistent with the measurements of k, based on heat-exchanger theory.

As discussed in §3.2.5, based on the good agreement between measurements of the interior flow and the predictions of heat-exchanger theory, we expect the asymptotic exponent for the scaling $k(Ra)$ to be bounded above by 0.5. Otherwise, horizontal diffusion ($\sim k^2/Ra$) would become stronger than vertical advection asymptotically, and the convective heat transfer would vanish as $Ra \to \infty$. A plausible prediction based on the measurements in this paper is therefore that the asymptotic scaling is $k \sim Ra^{0.5}$, although calculations at higher values of Ra would be required to confirm this. Certainly, the scaling appears to be stronger than the two-dimensional scaling of $k \sim Ra^{0.4}$, and the question remains as to why this difference exists. One theory that has been suggested for the physical control of the wavenumber $k(Ra)$ is that k is determined by the smallest length scale, or 'minimal flow unit', for which the flux remains independent of aspect ratio (Wen *et al.* 2013). Interestingly, this theory predicts a scaling of $k \sim Ra^{0.5}$ for steady two-dimensional convection (Corson 2011). Hewitt *et al.* (2013*b*) suggested that the reason the measured scaling in two dimensions is weaker than this is because it is constrained by the stability of the interior columnar flow. It seems likely, therefore, that a stability analysis of the three-dimensional heat-exchanger flow could shed light on the reason for the different scalings for k in two and three dimensions. Such an analysis is planned for future work.

Acknowledgements

REFERENCES

AHLERS, G., GROSSMANN, S. & LOHSE, D. 2009 Heat transfer and large scale dynamics in turbulent Rayleigh–Bénard convection. *Rev. Mod. Phys.* **81**, 503–537.

BICKLE, M. J. 2009 Geological carbon storage. *Nature Geosci.* **2**, 815–819.

BRIAN, P. L. T. 1961 A finite-difference method of high-order accuracy for the solution of three-dimensional transient heat conduction problems. *AIChE J.* **7**, 367–370.

CORSON, L. T. 2011 Maximising the heat flux in steady unicellular porous media convection. In *Proceedings of the 2011 Geophysical Fluid Dynamics Summer Program, Woods Hole Oceanographic Institution*, pp. 389–412.

CROSS, M. C. & HOHENBERG, P. C. 1993 Pattern formation outside of equilibrium. *Rev. Mod. Phys.* **65**, 851–1112.

E, W. & LIU, J. G. 1997 Finite difference methods for 3D viscous incompressible flows in the vorticity-vector potential formulation on nonstaggered grids. *J. Comput. Phys.* **138**, 57–82.

ELDER, J. W. 1967 Steady free convection in a porous medium heated from below. *J. Fluid Mech.* **27**, 29–48.

FU, X., CUETO-FELGUEROSO, L. & JUANES, R. 2013 Pattern formation and coarsening dynamics in three-dimensional convective mixing in porous media. *Phil. Trans. R. Soc.* A **371**, 20120355.

GRAHAM, M. D. & STEEN, P. H. 1994 Plume formation and resonant bifurcations in porous-media convection. *J. Fluid Mech.* **272**, 67–89.

HEWITT, D. R., NEUFELD, J. A. & LISTER, J. R. 2012 Ultimate regime of high Rayleigh number convection in a porous medium. *Phys. Rev. Lett.* **108**, 224503.

HEWITT, D. R., NEUFELD, J. A. & LISTER, J. R. 2013a Convective shutdown in a porous medium at high Rayleigh number. *J. Fluid Mech.* **719**, 551–586.

HEWITT, D. R., NEUFELD, J. A. & LISTER, J. R. 2013b Stability of columnar convection in a porous medium. *J. Fluid Mech.* **737**, 205–231.

HOLST, P. H. & AZIZ, K. 1972 Transient three-dimensional natural convection in confined porous media. *Intl J. Heat Mass Transfer* **15**, 73–90.

HOWARD, L. N. 1964 Convection at high Rayleigh number. In *Applied Mechanics, Proc. 11th Intl Cong. Appl. Math.* (ed. H. Görtler), pp. 1109–1115.

HUPPERT, H. E. & NEUFELD, J. A. 2014 The fluid mechanics of carbon dioxide sequestration. *Annu. Rev. Fluid Mech.* **46**, 255–272.

KADANOFF, L. P. 2001 Turbulent heat flow: structures and scaling. *Phys. Today* **54**, 34–39.

KIMURA, S., SCHUBERT, G. & STRAUS, J. M. 1989 Time-dependent convection in a fluid-saturated porous cube heated from below. *J. Fluid Mech.* **207**, 153–189.

LAPWOOD, E. R. 1948 Convection of a fluid in a porous medium. *Math. Proc. Cambridge Philos. Soc.* **44**, 508–521.

LISTER, C. R. B. 1990 An explanation for the multivalued heat transport found experimentally for convection in a porous medium. *J. Fluid Mech.* **214**, 287–320.

METZ, B., DAVIDSON, O., DE CONINCK, H. C., LOOS, M. & MEYER, L. 2005 IPCC special report on carbon dioxide capture and storage. Cambridge University Press.

NIELD, D. A. & BEJAN, A. 2006 *Convection in Porous Media*. 3rd edn Springer.

OTERO, J., DONTCHEVA, L. A., JOHNSTON, H., WORTHING, R. A., KURGANOV, A., PETROVA, G. & DOERING, C. R. 2004 High-Rayleigh-number convection in a fluid-saturated porous layer. *J. Fluid Mech.* **500**, 263–281.

PAU, G. S. H., BELL, J. B., PRUESS, K., ALMGREN, A. S., LIJEWSKI, M. J. & ZHANG, K. 2010 High-resolution simulation and characterization of density-driven flow in CO_2 storage in saline aquifers. *Adv. Water Resour.* **33**, 443–455.

SCHUBERT, G. & STRAUS, J. M. 1979 Three-dimensional and multicellular steady and unsteady convection in fluid-saturated porous media at high Rayleigh numbers. *J. Fluid Mech.* **94**, 25–38.

STRAUS, J. M. & SCHUBERT, G. 1979 Three-dimensional convection in a cubic box of fluid-saturated porous material. *J. Fluid Mech.* **91**, 155–165.

STRAUS, J. M. & SCHUBERT, G. 1981 Modes of finite-amplitude three-dimensional convection in rectangular boxes of fluid-saturated porous material. *J. Fluid Mech.* **103**, 23–32.

WEN, B., CHINI, G. P., DIANATI, N. & DOERING, C. R. 2013 Computational approaches to aspect-ratio-dependent upper bounds and heat flux in porous medium convection. *Phys. Lett.* A **377**, 2931–2938.